OUKA
The University of Osaka
Institutional Knowledge Archive

Title	Unsteady analysis of non-isothermal natural ventilation airflow using domain decomposition technique with LES
Author(s)	Matsubara, Toru; Kobayashi, Tomohiro; Yamanaka, Toshio et al.
Citation	Building and Environment. 2024, 262, p. 111763
Version Type	VoR
URL	https://hdl.handle.net/11094/98159
rights	This article is licensed under a Creative Commons Attribution 4.0 International License.
Note	

The University of Osaka Institutional Knowledge Archive : OUKA

https://ir.library.osaka-u.ac.jp/

The University of Osaka

Building and Environment 262 (2024) 111763

Contents lists available at ScienceDirect

Building and Environment

journal homepage: www.elsevier.com/locate/buildenv

Unsteady analysis of non-isothermal natural ventilation airflow using domain decomposition technique with LES

Toru Matsubara [a,*], Tomohiro Kobayashi [a], Toshio Yamanaka [a], Noriaki Kobayashi [a], Narae Choi [b], Shohei Miyazawa [a], Zitao Jiang [a], Chisato Tambara [c]

[a] Department of Architectural Engineering, Graduate School of Engineering, Osaka University, Osaka, 565-0871, Japan
[b] Department of Architecture, Faculty of Science and Engineering, Toyo University, Tokyo, Japan
[c] Obayashi Corporation, Tokyo, Japan

ARTICLE INFO

Keywords:
Large eddy simulation
Domain decomposition technique
Non-isothermal simulation
Wind tunnel experiment

ABSTRACT

A Large Eddy Simulation (LES) can predict an unsteady airflow with high accuracy. However, the application of LES to indoor airflows is difficult because of the large computational burden of the coupled simulation of both the indoor/outdoor domains. To address this issue, a domain decomposition technique (DDT) was proposed so that the outdoor simulation results could be applied as boundary conditions for the indoor air simulation by decoupling the indoor/outdoor domains. However, most previous studies have only investigated the applicability of DDT under steady-state and isothermal conditions. In an actual natural ventilation design, if buoyancy force is expected as the primary natural ventilation driving force, the temperature difference between indoor/outdoor cannot be neglected. This study aimed to validate the DDT under non-isothermal conditions. First, wind tunnel experiments were conducted on an isolated building under non-isothermal conditions to obtain data for the computational fluid dynamics boundary conditions and accuracy verification. The wind pressure coefficient, velocity distribution, and temperature distribution were measured during the experiment. Then, unsteady analysis (i.e., whole domain simulation) was performed using LES to reproduce the wind tunnel experiment. Finally, DDT was applied to the Large Eddy Simulation, and its accuracy was verified by comparing the velocity distribution, temperature, and airflow rate between the whole domain and DDT. As a result, in the present study where the total number of grids in the entire domain was approximately 10 times that in the indoor domain, DDT exhibited good accuracy, and decreased the computational load by over 70 %.

Nomenclature

Symbols	Description	Units
C_p	Wind pressure coefficient	[−]
P_w	Static pressure at the wall surface	[Pa]
P_{ref}	Reference static pressure	[Pa]
v_{ref}	Building height velocity	[m/s]
ρ	Air density	[kg/m^3]
T	Temperature	[K]
W	Indoor heat generation rate	[W]
C_p	Specific heat capacity	[J/kgK]
Q_i	Instantaneous airflow rate	[m^3/s]
U	Heat transfer coefficient	[W/m^{2}K]
A_s	Model surface area	[m^2]
C_d	Discharge coefficient	[−]
$(C_dA)_{connected}$	Connected value of the effective opening area	[m^2]

(*continued on next column*)

(*continued*)

Symbols	Description	Units
ΔP	Pressure difference	[Pa]
ΔC_p	Wind pressure coefficient difference	[−]
$\Delta\rho$	Density difference	[kg/m^3]
g	Gravitational acceleration	[m/s^2]
Δh	Difference in height between openings	[m]
A	Opening area	[m^2]
v_n	Wind velocity normal to the opening	[m/s]
$v_{p(y)}$	Wind velocity parallel to the opening (y-direction)	[m/s]
$v_{p(z)}$	Wind velocity parallel to the opening (z-direction)	[m/s]
Ar	Archimedes number	[−]
v_{room}	Wind velocity into the room	
β	Coefficient of cubic expansion	[1/T]
ΔT	Temperature difference	[K]
$L_{building}$	Characteristic length of the building	[m]

(*continued on next page*)

* Corresponding author.
E-mail address: matsubara_toru@arch.eng.osaka-u.ac.jp (T. Matsubara).

https://doi.org/10.1016/j.buildenv.2024.111763
Received 19 December 2023; Received in revised form 19 May 2024; Accepted 20 June 2024
Available online 21 June 2024
0360-1323/© 2024 The Authors. Published by Elsevier Ltd. This is an open access article under the CC BY license (http://creativecommons.org/licenses/by/4.0/).

(*continued*)

Symbols	Description	Units
$L_{opening}$	Characteristic length of the opening	[m]
$Q_{predicted}$	Predicted value of airflow rate	[m^3/s]
P_{wd}	Windward total pressure	[Pa]
P_{Ld}	Leeward total pressure	[Pa]
C	Courant number	[−]
υ	Kinematic viscosity coefficient	[m/s]
Re	Building *Re*: Building height Reynolds number	[−]
	Opening *Re*: Opening Reynolds number	[−]
Δt	Time step size	[s]
Δl	Cell size	[m]
$v_{normalized}$	Normalized velocity	[−]
v_x	X-component velocity	[m/s]
v_z	Z-component velocity	[m/s]
$\overline{C_p}$	Time-averaged wind pressure coefficient	[−]
$Q_{in\text{-}out}$	Airflow rate from indoor to outdoor	[m^3/s]
$Q_{out\text{-}in}$	Airflow rate from outdoor to indoor	[m^3/s]
u'	Fluctuating component of velocity	[m/s]
τ	Time lag	[s]
t	Time	[s]
R	Autocorrelation coefficient	[−]
Λ	Integral time scale	[s]
λ	Turbulence length scale	[m]
C_D	Empirical coefficient	[−]
$\overline{u}$	Average velocity	[m/s]
	- subscript -	
in	Indoor	
out	Outdoor	
i	Instantaneous	

1. Introduction

In recent years, natural ventilation has been considered as an effective energy-saving approach. Two types of driving forces play a role in natural ventilation: wind-induced ventilation, driven by wind pressure differences between openings, and buoyancy-driven ventilation, driven by indoor/outdoor temperature differences [1,2]. Natural ventilation has primarily been introduced into building design because it reduces energy consumption and improves indoor air quality [3]. To use natural ventilation, it is necessary to accurately predict the ventilation rate, airflow characteristics, and indoor/outdoor temperature differences during the building design phase [4]. Three methods are used to achieve these objectives, namely: 1) field measurements: a performance evaluation by measurement in an actual building [5–9]; 2) wind tunnel experiments: data are acquired using a wind tunnel with a reduced-scale model; however, this requires large laboratory facilities, high cost, time, and a variety of equipment [10–17]; 3) computational fluid dynamics (CFD): a simulation with 3D models on a computer, which boasts easily changeable parameters, low cost, and flexibility to obtain data from any place in the simulation domain. Since the 1960s, CFD has been developed as a fluid dynamics method [18–23].

Furthermore, several methods exist for simulating turbulent flows. The most accurate approach is the direct numerical simulation (DNS), in which the full Navier–Stokes equations are directly calculated using an extremely fine mesh from the smallest to the largest eddies of the given airflow. A second method is the Large Eddy Simulation (LES), a type of CFD that performs unsteady airflow analysis with high accuracy [24]. This method was first proposed by Smagorinsky in 1963 [25]. In LES, the large-scale motions of turbulent flow are directly solved, and only small-scale motions are modeled using a sub-grid scale model. Recently, guidelines that include LES analysis of outdoor airflow have been developed, and the use of LES for ventilation analysis is expected to expand in the future [26–32].

The Reynolds Averaged Navier-Stokes (RANS), which concerns the Reynolds-averaged airflow field, is widely used for ventilation simulations. It can reproduce an airflow field with a lower computational load than LES models. However, LES is required to simulate natural ventilation with continuous changes in wind velocity and direction. The RANS and LES methods have been compared in previous studies. Cheng et al. [33] showed the comparison of flow simulations computed by the two-equation turbulence models (the standard k-ε model, renormalized k-ε model, standard k-ω model, and Shear Stress Transport k-ω model) as well as LES and wind tunnel experiment data. Cheng et al. [34] performed a simulation to reproduce the wind tunnel experiment conducted by Meinders [35] using RANS and LES. The complex features of the fully developed flow within and above an array of cubes were better reproduced with LES than with RANS despite the disadvantage of much greater computation times. Xie et al. [36] showed a comparison of LES with three RANS models (the standard k-ε, modified k-ε, and Reynolds stress model – hereinafter referred to as RSM) under much higher Reynolds number conditions. Compared with the experimental data [37], the RSM yielded the most accurate pressure profiles among the three RANS models. However, the unsteady RANS method could not be successfully applied to highly turbulent flows above the canopy because of the lack of significant scale separation and periodicity. Zheng et al. [38] compared the natural ventilation rate and velocity between RANS and LES for a building with balconies. The results suggested that the use of the RANS instead of the LES can result in underestimated ventilation rates and wind velocity ratios. Tominaga et al. [39,40] demonstrated the accuracy of LES around a simple building model through the velocity distribution, turbulence kinetic energy distribution, and concentration measurements. LES can calculate instantaneous fluctuations that cannot be obtained using the RANS model. The horizontal diffusion of the concentration was well reproduced by LES owing to the unsteady concentration fluctuation. Adachi et al. [41] reported the results of the velocity fields within a cross-ventilation model sheltered by block arrays using LES. Simultaneous observations of the outdoor and indoor velocities indicated that the change in the outdoor flow patterns caused a dramatic change in the indoor velocity distributions. Based on these previous studies, RANS is a widely used model for predicting indoor airflow in ventilation design. In addition, LES can simulate unsteady flows with high accuracy; however, its computational load is significantly higher than that of RANS.

As mentioned previously, LES has the disadvantage of using a large computational load [42,43]. A general natural ventilation simulation using LES requires a simulation domain that includes both the building's interior and outdoor areas. This results in a large computational load and the analysis requires an enormous amount of time. Therefore, to use LES on a practical level, it is necessary to establish a method that reduces the computational load while preserving the method's high accuracy. Domain decomposition technique (DDT) is a promising method to reduce computational load, and only simulate the indoor airflow by using the numerical results of outdoor airflow. The use of DDT is expected to significantly reduce the computational load [44]. In a study by Kurabuchi et al. [45], DDT was applied to the RANS model for wind-induced natural ventilation under isothermal conditions. They applied the DDT using a local dynamic similarity model (LDSM) to modify the discharge coefficients of the openings [46,47]. In reality, the buoyancy force is also an important driving force for natural ventilation [48–52]; however, the application of DDT under non-isothermal conditions has not been investigated to date. In addition, the applicability of DDT in LES has not been validated in previous studies. To bridge those research gaps, in this study, DDT was applied to an LES in a non-isothermal environment.

The primary goal of the present research is to validate the accuracy of DDT for LES under non-isothermal conditions by comparing simultaneous indoor/outdoor simulations (whole domain simulation) with an indoor-only simulation using DDT. This paper describes the results of applying DDT to unsteady simulations by LES under non-isothermal conditions using a reduced model used in wind tunnel experiments. Section 2 introduces the theory and processes of DDT. Section 3 describes the wind tunnel experiments, Section 4 illustrates the CFD methodologies, and Section 5 summarizes the main findings of the present research and the limitations of the DDT.

2. Domain decomposition technique with LES

The unsteady analysis procedure using DDT is shown in Fig. 1 and consists of three steps. Although the detailed calculation setting is shown later in Sections 3.2.1 and 3.2.2, the basic concept of the technique is introduced here.

Step 1: An outdoor simulation using a sealed model without openings is conducted under isothermal conditions. In this simulation, the instantaneous static pressure and wind velocity components parallel to the wall surface were obtained to acquire the boundary conditions for the indoor simulation in the DDT. Instantaneous static pressures on the wall (wind pressure) are obtained at the position where supposed to be the center of the opening. The instantaneous wind velocity components parallel to the wall near the assumed opening position were also obtained. The reference static pressure is monitored on the windward side. The Instantaneous wind pressure coefficient at each opening point was calculated using Eq. (1).

$$C_{pi} = \frac{P_{wi} - P_{ref}}{\frac{1}{2}\rho_{out}\left(v_{ref}\right)^2} \tag{1}$$

where C_{pi} is the instantaneous wind pressure coefficient [−], ρ_{out} is the density of the outdoor air [kg/m^3], v_{ref} is the reference velocity at building height in the approaching flow [m/s], P_{wi} is the instantaneous static pressure on the wall [Pa], P_{ref} is the static pressure on the windward side [Pa].

Step 2: The instantaneous airflow rate induced by the wind and buoyancy forces at each time step is calculated by applying the heat balance equation (Eq. 2), the orifice equation (Eq. 3), and the pressure difference equation (Eq. 4) into an iterative calculation: In these equations, buoyancy-driven flow is defined as positive (upward direction in the present study), and the sign of the wind pressure coefficient difference is defined as positive when it assists buoyancy-induced ventilation. In the iterative calculations, the discharge coefficient at the orifice was maintained at 0.67, and the initial indoor temperature was set to the same value as the outdoor temperature and was assumed to be uniform. Next, the instantaneous wind velocity perpendicular to the opening, which is the airflow divided by the opening area, was calculated at each time step using Eq. (5).

$$T_{in} - T_{out} = \frac{W}{Cp\rho_{out}Q_i + UA_s} \tag{2}$$

$$Q_i = (C_dA)_{connected}\sqrt{\frac{2}{\rho}|\Delta P_i|} \tag{3}$$

$$\Delta P_i = \frac{\Delta C_{pi}\rho\left(v_{ref}\right)^2}{2} + \Delta\rho g\Delta h \tag{4}$$

$$v_{ni} = \frac{Q_i}{A} \tag{5}$$

where T_{in} is the indoor temperature [K], T_{out} is the outdoor temperature [K], W is the indoor heat generation rate [W], Cp is specific heat capacity [J/kgK], ρ_{out} is outdoor air density [kg/m^3], Q_i is the instantaneous airflow rate [m^3/s]. U is average heat transfer coefficient of the wall [W/m^{2}K], A_s is the model surface area [m^2], $(C_dA)_{connected}$ is the connected value of the effective opening area [m^2], ΔP_i is the instantaneous pressure difference through a total flow path [Pa], ΔC_{pi} is the wind pressure coefficient difference between openings [−], $\Delta\rho$ is the density difference [kg/m^3], g is the gravitational acceleration [m/s^2], Δh is the difference in height between openings [m], v_{ni} is the instantaneous velocity component normal to the opening [m/s], and A is the opening area [m^2]

Step 3: To analyze the indoor airflow field, the instantaneous velocity components that were normal to the opening from Step 2 and parallel to the wall from Step 1 were provided at the openings as inlet/outlet boundary conditions. These velocity components were given as the instantaneous boundary condition of the velocity at each time step, and the procedure was repeated throughout the unsteady calculation period. Thus, an unsteady DDT simulation was performed using LES.

To examine the accuracy of DDT with the scheme shown above, LES calculations with and without DDT are compared in the following section. Here, the simulation without DDT indicates that it analyzes both the indoor/outdoor domains simultaneously and is referred to as the whole domain simulation. In other words, the present study verifies the accuracy of the DDT by assuming the whole domain simulation as the true value, as shown in Section 4.2. To achieve this, the accuracy of the whole domain simulation was first verified by wind tunnel experiments, and the results are presented in Section 4.1. In this validation procedure, wind pressure, room temperature, and airflow field were measured and compared with the CFD results.

3. Methodology

The details of the methodologies for the wind tunnel experiment, whole domain simulation, and indoor airflow simulation with DDT are described in this section.

3.1. Wind tunnel experiment

The purpose of the wind tunnel experiment was to obtain experimental data for the validation of the LES by comparing the results of the whole domain simulation. In the wind tunnel experiment, a rectangular 1:10 scale model with a single room was exposed to boundary layer flow. The boundary layer flow velocity profile was first measured, followed by the wind pressure coefficient, indoor temperature distribution, and indoor velocity distribution. All measurements were conducted thrice, and the average values were adopted as the experimental results. Here, the velocity profiles of the boundary layer flow and heat flux are given as the boundary conditions of the CFD, as described in Section 3.2. The experiments are illustrated in Fig. 2. More detailed explanations for each experiment are provided in the following sections.

3.1.1. Summary of the wind tunnel

The wind tunnel experiment was conducted in a wind tunnel at Osaka University, as shown in Fig. 3. The facility has a test section with a length of 9.5 m with a cross-section of 1.8 m (width) × 1.6 m (height). It is possible to change the type of wind tunnel, that is, open- or closed-circuit types. The wind velocity in the wind tunnel was set at 1.0 m/s at a height of 1000 mm above the floor but was also set at 10 m/s only when measuring the wind pressure and boundary layer velocity profile, as described below. During wind pressure measurement, the approaching wind velocity was simultaneously measured using a pitot tube, as shown in Fig. 3. In other measurements, approaching velocity was monitored by the ultrasonic anemometer to set the velocity at 1.0 m/s on the leeward of the model. Fig. 4 shows the vertical profile of the approach flow velocity and the turbulence intensity measured using a hot-wire anemometer with an I-type probe (0251R-T5, Kanomax) at 1.0 kHz for 60 s without the model setup. The wind velocity was normalized to that at a height of 600 mm. The results show that the boundary layer flow follows the power law of 1/3.73 and 1/4.20 for the 1.0 m/s and 10 m/s conditions, respectively.

3.1.2. Case and experimental conditions

Table 1 summarizes the experimental conditions and corresponding assumed full-scale conditions. Pressure differences owing to wind and buoyancy forces were applied in the same direction. Fig. 5 shows the

Step 1 : Outdoor analysis with sealed building model to obtaion instantaneous value (P_{wi}, P_{refi}, v_{pi})

Start

- External flow field is analyzed by RANS calculation, where a building is simulated as a sealed model, and the result is used as initial condition for LES
- Turbulence model is switched to LES, and preliminary calculation is run （0.001 [s/step] 20,000 [step]=20[s]）
- Main LES calculation for the sealed model is run （0.001 [s/step] × 60,000 [step]=60[s]）

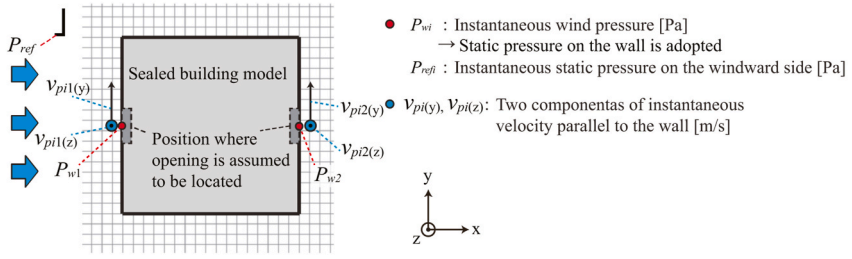

- Obtain instantanenous value for P_{wi}, P_{refi}, $v_{pi(1)}$ and $v_{pi(2)}$ in time series throughout the main calculation period (60.0[s])

End

Step2 : Caluculation of instantaneous velocity component normal to openning

Start

- Calculate the of instantaneous wind pressure coefficient on each openning opsition

$$C_{pi} = \frac{P_{wi} - P_{ref}}{\frac{1}{2}\rho_{out}(v_{ref})^2}$$

- Renewal of instantaneous internal temperature T_{in} [K] (Initial value : outdoor temperapture)
- Caluclation of airflow rate

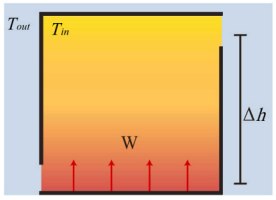

$$\Delta\rho = \frac{353.25}{T_{out}} - \frac{353.25}{T_{in}} \quad [\mathrm{kg/m^3}]$$

$$Q_i = (C_dA)_{connected}\sqrt{\frac{2}{\rho}\Delta P} \quad [\mathrm{m^3/s}]$$

$$|\Delta P| = \left|\frac{\Delta C_{pi}\rho(v_{ref})^2}{2} + \Delta\rho g\Delta h\right| \quad [\mathrm{Pa}]$$

$$T_{in} - T_{out} = \frac{W}{Cp\rho Q_i + UA_s} \quad [\mathrm{K}]$$

C_{pi} : Wind pressure coeffcient [-]
Q_i : Airflow rate [m³/s]
$(C_dA)_{connected}$: Connected effective opening area [m²]
ρ_{out} : Density of air [kg/m³]
ΔP : Pressure difference [Pa]
v_{ref} : Building height velocity [m/s]
ΔC_{pi} : Wind pressure coeffcient difference [-]
$\Delta\rho$: Density difference [kg/m³]
C_d : Discharge coefficient [-]

g : Gravitational acceleration [m/s²]
Δh : Difference in height between openings [m]
T_{out} : Outdoor temperature [K]
T_{in} : Indoor temperature [K]
W : Indoor heat generation rate [W]
Cp : Specific heat capacity [J/kgK]
U : Heat transfer coefficient [W/m²K]
A_s : Model surface area [m²]

Sequential caluclation procedure

Update T_{in}

Converged? No

Yes

- Instantaneous flow rate of each opening is obtained throughout main calculation period of sealed building simulation (60.0 [s]), and the instantaneous velocity component normal to the opening, v_{ni} [m/s], is given as $v_{ni} = Q_i / A$

End

Step3 : Indoor simulaiton using LES with domain decomposition technique

Start

- Indoor calculation domain is simulated where opening is inlet/outlet boundary

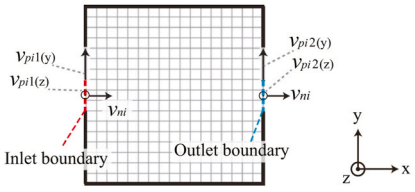

- Initial condition is calculated by RANS model of which boundary condition is obtained based on RANS result of Step 1 and Step 2
- Turbulence model is switched to LES. For both inlet and outlet boundary condition, three components of instantaneous velocity are given as followings;
  - Velocity component normal to the opening; v_{ni} obtained from Step 2
  - Two velocity components parallel to the opening; v_{pi1} and v_{pi2} obtained from Step 1
- Preliminary LES calculation for indoor flow is run （0.001 [s/step] × 20,000 [step] = 20 [s]）
- Main LES calculation for indoor airflow is run (0.001 [s/step] × 60,000 [step] = 60 [s])

End

Fig. 1. Procedure of unsteady analysis using the domain decomposition technique with LES.

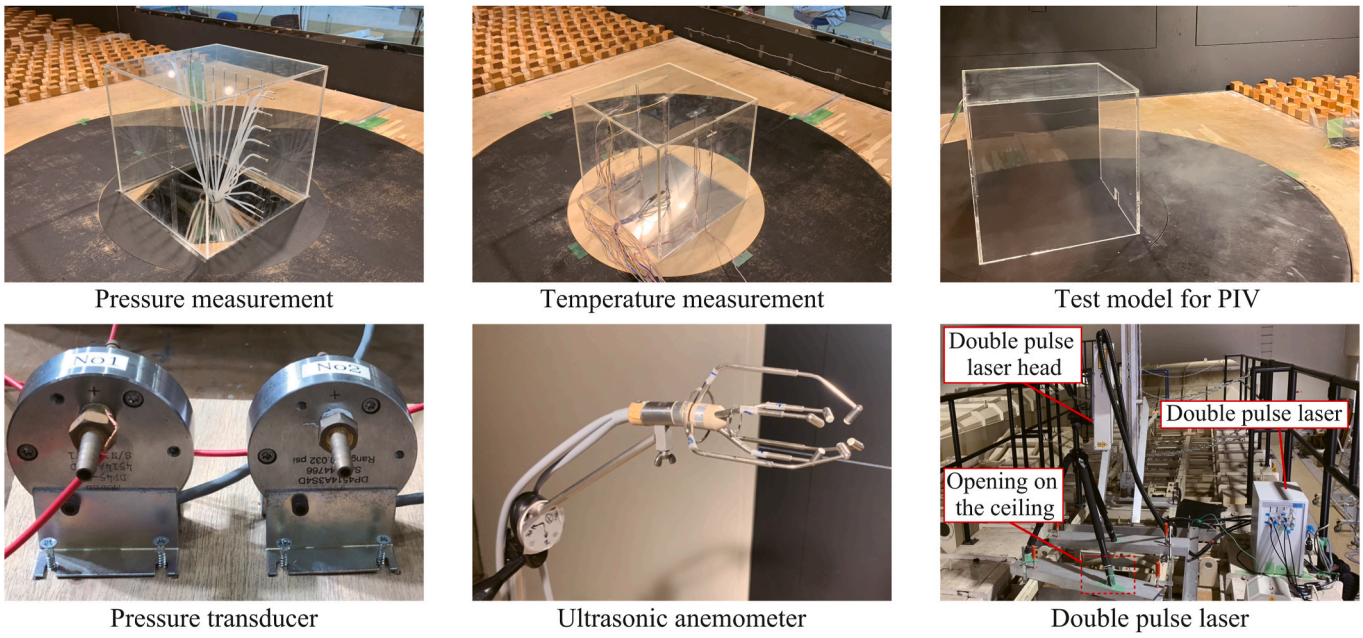

Fig. 2. Experiments and experimental equipment.

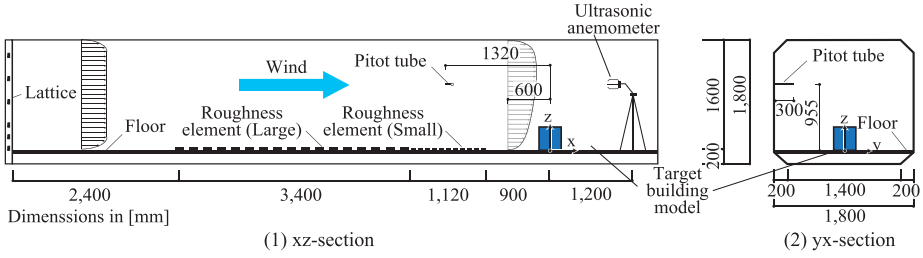

Fig. 3. Schematic of the wind tunnel test.

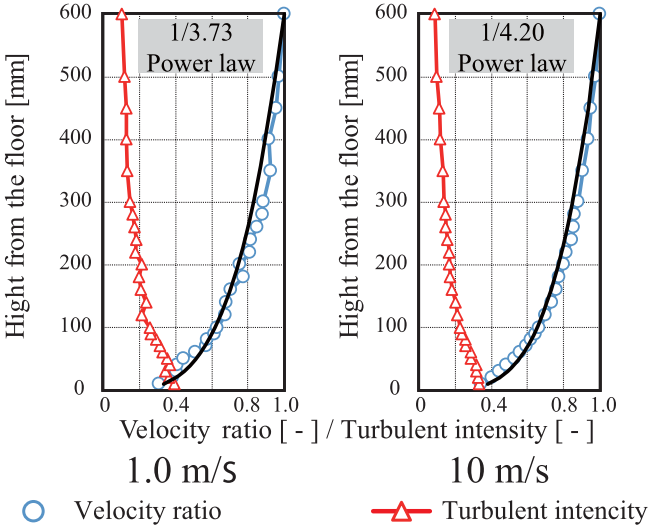

Fig. 4. Approaching flow of wind tunnel: (left) 1.0 m/s; (right) 10 m/s.

details of the proposed model. The scaled model used was a cubic shape with an external dimension of 300 mm, made of 5.0 mm-thick acrylic boards. It was assumed to have two openings (30 mm × 30 mm) at different heights (15 mm and 280 mm from the floor) on the center. The model was placed so that the openings were on the central yz-section of the wind tunnel. The floor surface of the model was made of an aluminum plate, and a silicone rubber heater and insulation material were placed underneath to create an indoor/outdoor temperature difference in the model. The indoor temperature was monitored at the center of the leeward opening, assuming it as the exhaust temperature. The outdoor temperature was monitored 600 mm upstream of the windward opening. Heat was generated by using a silicone rubber heater under the floor surface. The amount of generated heat was adjusted to achieve the desired room temperature.

To consider similarity, the Archimedes number (Ar) (Eq. (6)) was calculated using the indoor/outdoor temperature difference measured at the reference point. The opening velocity is calculated by dividing the airflow rate by the opening area. (Eq. (7)). The Reynolds number (Re) at the opening was calculated as follows: (8). Here, Re at the opening did not become as large as that in the full-scale condition. This is because Ar was assumed to be the most important factor for meeting the similarity to the full-scale condition.

$$Ar = \frac{g\beta L\Delta T}{v_{room}{}^2} = \frac{g\beta\Delta h(T_{in}\text{-}T_o)}{(Q_{predicted}/A)} \tag{6}$$

$$Q_{predicted} = (C_dA)_{connected}\sqrt{\frac{2}{\rho_{out}}|P_{wd}\text{-}P_{Ld} + (\rho_o\text{-}\rho_{in})g\Delta h|} \tag{7}$$

$$Opening\ Re = \frac{Q_{predicted}\ L_{opening}}{vA} \tag{8}$$

Table 1
Experimental conditions.

	Building height [m]	Building height velocity [m/s]	Outdoor temperature [°C]	Indoor temperature [°C]	Ar number	OpeningRe number	BuildigRe number
Full-scale	3.0	2.0	10.0	25.0	0.39	5830	4,00,000
Reduced scale	0.3	0.9	17.0	44.6	0.39	986	17,560

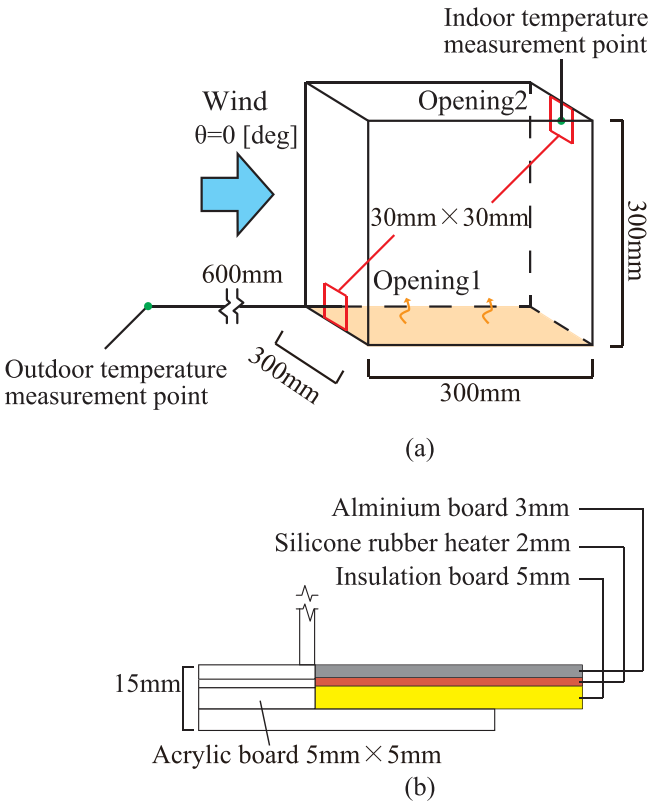

Fig. 5. Details of the model: (a) details of the model and temperature reference points; (b) details of heat generation.

$$Building\ Re = \frac{v_{ref}\ L_{building}}{\nu} \tag{9}$$

where $(C_dA)_{connected}$ is the connected value of the effective opening area [m^2], P_{Wd} and P_{Ld} are the wind pressures on the windward and leeward wall surfaces [Pa], β is the coefficient of cubic expansion [1/K], v_{room} is the velocity into the room [m/s], and $L_{opening}$ is the characteristic length of opening [m], $L_{building}$ is the characteristic length of building [m].

In this study, three types of experimental models composed of acrylic boards were used, as shown in Fig. 6, Fig. 7, and Fig. 8. The first was a sealed model without openings, as shown in Fig. 6. The other models are ventilation models with openings, as shown in Figs. 7 and 8. The wind pressure coefficient was measured using a sealed model, while the temperature distribution, floor heat flux, and indoor air velocity distribution were measured using a ventilation model.

3.1.3. Pressure measurement of sealed model

As mentioned above, three types of wind tunnel experiments were performed to obtain the experimental results to be compared with the LES for validation, and the boundary conditions of the LES with the domain composition technique. For wind pressure measurements, the mean static pressure at the model surface was measured using a sealed model as shown in Fig. 6 to obtain the wind pressure coefficient. The wind pressure coefficient can be calculated using Eq. (10).

$$C_p = \frac{P_s\text{-}P_{ref}}{\frac{1}{2}\rho_{out}\left(v_{ref}\right)^2} \tag{10}$$

where C_p is the wind pressure coefficient [−], ρ_{out} is the density of air [kg/m3], v_{ref} is the reference velocity at building height [m/s], P_s is the static pressure on the measurement point [Pa], and P_{ref} is the static pressure at the pitot tube [Pa].

A total of 22 measurement points were set up (nine points at 30 mm intervals on the windward and leeward surfaces of the model center section, and four points at the assumed opening locations (15 mm and 280 mm above the floor). In this setup, the wind velocity in the wind tunnel was set to 10 m/s, 1000 mm above the floor. The wind pressure was measured at 1.0 kHz for 60 s at each point using a pressure transducer (DP45, Validyne). The reference velocity for the wind pressure coefficient was the approach flow velocity at the building height (300 mm above the floor), and the reference static pressure in the wind tunnel was measured using a pitot tube, the position of which is shown in Fig. 3. In this experiment, the wind tunnel was operated as a closed-circuit.

3.1.4. Temperature measurement

The temperature inside the model and heat flux at the model floor were measured using the ventilation model shown in Fig. 7. The former was intended to obtain the experimental results required for CFD validation, and the latter was used to obtain the boundary conditions for the CFD. Air temperatures in the model were measured by thermocouples at three points in the vertical direction (75, 150, and 225 mm) and three positions along the central line of the model in the streamwise direction, that is, nine points in total. The inner surface temperatures of the floor and roof were measured at the center of the room. The heat flux on the floor was measured using a heat flux meter (Energy Eye-D0001, DENSO)

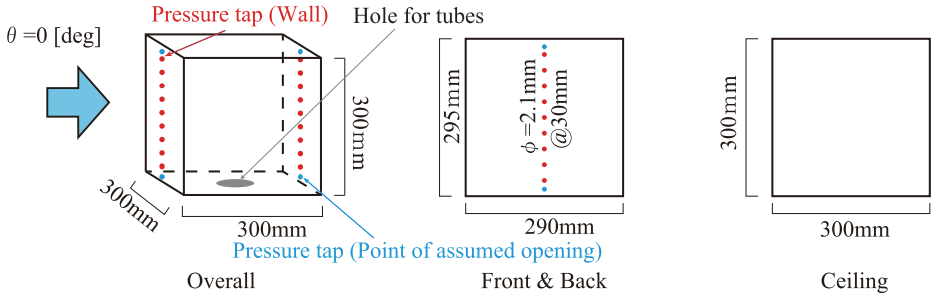

Fig. 6. Sealed model for pressure measurement.

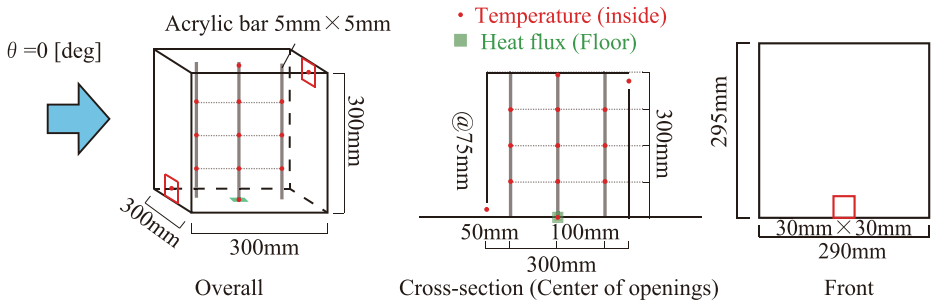

Fig. 7. Ventilation model for temperature and heat flux measurement.

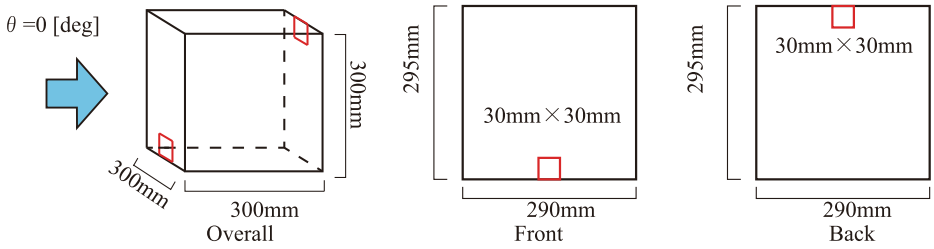

Fig. 8. Ventilation model for PIV measurement.

at the center of the floor surface. The measurement was started after it had reached a steady-state, and then a 10-min average of the temperatures measured at a frequency of 1.0 Hz at each point was taken. This sequence of measurements was repeated three times, and the average value was adopted as the steady-state temperature at each point. The wind tunnel was operated in closed-circuit mode during the experiment.

3.1.5. PIV measurement

Because we intended to compare the indoor airflow patterns in the CFD validation procedure, the indoor velocity distribution was measured by Particle Image Velocimetry (PIV) using the ventilation model shown in Fig. 8. Smoke was injected upstream of the model after confirming that the indoor temperature had reached a steady-state, and a double-pulse laser (DPIV-L50, Kanomax) installed above the model irradiated the laser sheet at 2.0 Hz over the center section of the model. A CCD camera (Image ProX 2 M, La Vision) was placed on the side of the wind tunnel and synchronized with a laser to capture images inside the model for 60 s using a program (Davis 8.3 La Vision). Thus, 120 sets of photos were obtained. The time interval between the two photographs was set to 1.0 ms. The camera resolution was 1600 × 1200 pixels. The direct cross-correlation method was used as an algorithm for PIV processing, and the accuracy was improved using the recursive correlation method. The first pass of the interrogation window size was 48 × 48 pixels and the second pass was 32 × 32 pixels. To exhaust the injected smoke, the wind tunnel was operated in an open-circuit mode during the experiment.

3.2. CFD

The purpose of this paper was to validate the accuracy of the DDT by comparing whole domain simulation results. First, the whole domain simulation that reproduced the wind tunnel experiment was performed under non-isothermal conditions. Because the accuracy of this whole domain simulation should also be verified, the results of the experiment and the whole domain simulation were first compared. Through this procedure, the whole domain analysis is validated and could be regarded as a reliable result. Then, the simulations with only the indoor domain were conducted using DDT and compared with the whole domain simulation. In this section, the LES methodologies for the whole domain and DDT, composed of outdoor/indoor simulations, are described.

3.2.1. Whole domain simulations

The whole domain simulation was performed under non-isothermal conditions. The building model had a cubic shape with external dimensions of 300 mm and a wall thickness of 5 mm. The model had square openings of 30 mm on the windward and leeward sides. The simulations were conducted for two cases: one with a wind direction of 0°, which was the same condition as in the wind tunnel experiment (Case 1). In Case 1, the pressure differences owing to the wind force and buoyancy act in the same direction. In Case 2, the wind direction was set to 180°, and the wind and buoyancy acted in opposite directions. Case 1 was analyzed as a basic non-isothermal ventilation airflow field to verify the accuracy of DDT, where another purpose to validate the whole domain analysis was also included. Then, Case 2 was calculated to verify DDT in the flow field with other characteristics, where the airflow field becomes unstable, and LES becomes effective, making DDT highly significant. For this reason, Case 2, which was not conducted in the experiment, was set up in the CFD. Fig. 9(a) shows the computational domain and mesh layout for Case 1. The computational domain has an xz-section with a length of 4.8 m and a yz-section of 1.8 m (width) × 1.6 m (height). The total number of cells was 1,133,140. In a preliminary study, several grid systems were studied with fine, medium, and coarse grids, and the coarse mesh system was finally adopted because no significant differences were observed. The coarse mesh was generated based on the number of divisions, 30 (width), 30 (height), and 5 (thickness) divisions. Throughout the main calculation period described below, the three components of the instantaneous air velocity were monitored at 149 points (99 points on the xz-section in the indoor area and 25 points at each opening) to validate the DDT.

The instantaneous inlet condition was created by applying Smirnov's method [53,54] based on the experimental values shown in Fig. 4 for a wind velocity of 1.0 m/s. A coupled radiation analysis was performed, and the wall emissivity was set to 0.9 uniformly. Table 2 lists the thermal boundary conditions used in this study. The inlet boundary condition was set at 17.4 °C. The heat fluxes from the floor were uniformly assigned the same values as those in the experimental results. The thermal boundary conditions on the interior surface of the model were determined by considering the total thermal conductance of the wall, as listed in Table 2 and shown in Fig. 10. This indicates that the heat inside

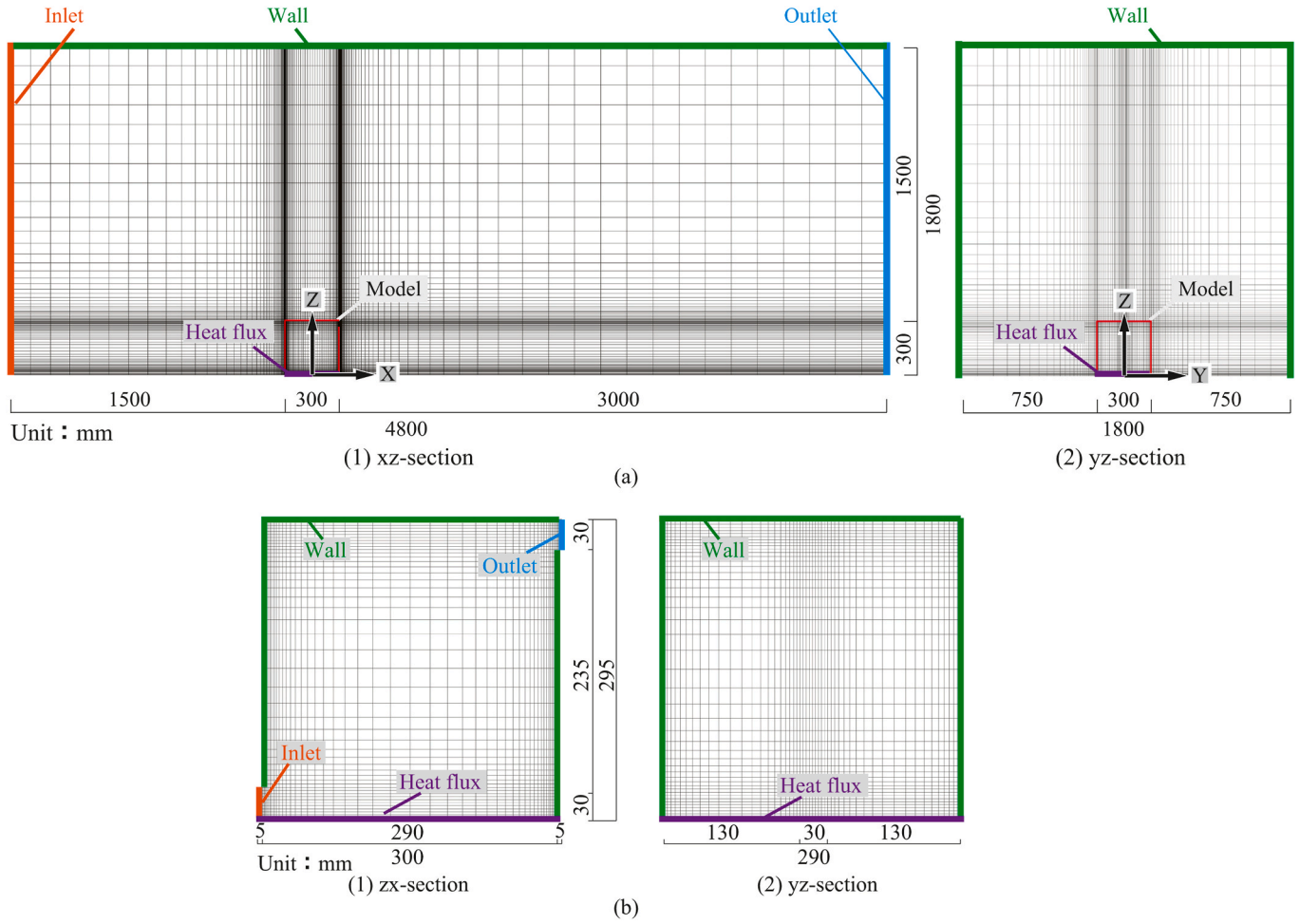

Fig. 9. Computational domain: (a) whole domain; (b) indoor domain.

Table 2
Thermal boundary condition.

Inlet	Floor	Interior model surface	Exterior model surface
Temperature17.4 [°C]	Uniform heat flux from wind tunnel experiment 1077.5 [W/m2]	Given considering total thermal conductunce of the wall ※Assumption 1) Interior surface Temperature wall function 2)Thermal conductivity within the walls Thermal conductivity: 0.19 [W/mK] (0.005 [m]), Density: 1186.43 [kg/m3], Specific heat capacity: 1470 [J/kgK] 3) Exterior surface Convective heat transfer coefficient and temperature Leeward wall: 6.0 [W/m2K] Other walls: 10 [W/m2K] Temperature 17.4 [°C]	Adiabatic

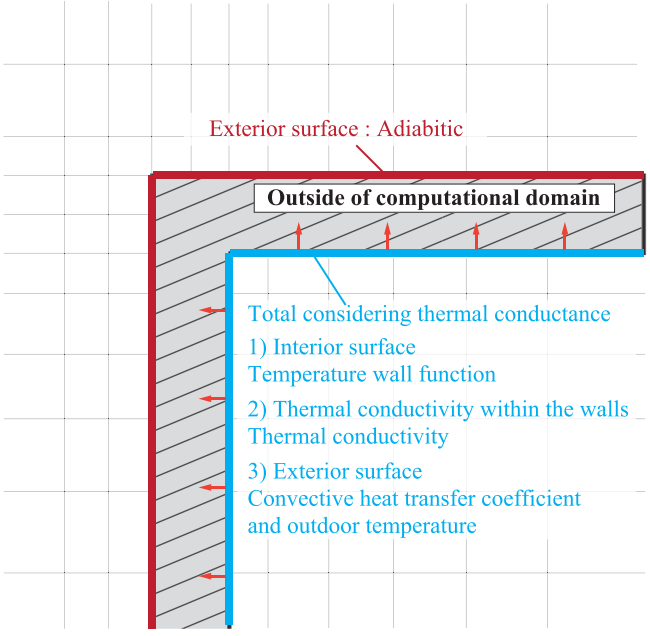

Fig. 10. Thermal boundary condition.

the test model is removed not only by advection of the ventilation flow but also through the wall. An adiabatic thermal boundary condition was applied to the exterior surface of the model. Strictly speaking, the heat removed from the model into the outdoor domain through the model wall should be considered; however, this was ignored, assuming that its influence on the outdoor temperature was almost negligible.

Table 3 summarizes the whole domain simulations. The results of the RANS simulation with the same mesh were used as initial values, where the RSM was applied as the turbulence model, the Semi-Implicit Method for Pressure-Linked Equations (SIMPLE) algorithm was applied for pressure–velocity coupling, Quadratic Upstream Interpolation for Convective Kinematics (QUICK) was applied for discretization scheme for advection term. In the RANS simulation, the approach flow of 1.0 m/s shown in Fig. 3 was given as an inflow boundary condition and the initial indoor temperature was set at 45 °C. For the LES, the Smagorinsky-Lilly model was used, and the Pressure-Implicit with Splitting of Operators (PISO) algorithm was applied for pressure velocity coupling. The Central Differencing Scheme was adopted as the spatial discretization scheme. The time step size was set at 0.001 s (1.0 kHz) to maintain the Courant below 1.0, as calculated by Eq. (11).

$$Courant = \frac{v\Delta t}{\Delta l} \tag{11}$$

where *Coutrant* is the courant number [−], v is the average velocity magnitude at each cell [m/s], Δt is the time step size [s] and Δl is the characteristic length of each cell [m].

After the LES calculation started, the first 20 s was regarded as the pre-conditioning period, which was the transition period from the RANS results to the LES, and the results obtained during this period were discarded. The following 60 s were regarded as the main calculation period, and the obtained results were used for data collection. The time step size was set at 0.001 in the pre-conditioning period (0.001 s × 20,000 time steps = 20 s) and the main calculation period (0.001 s × 60,000 time steps = 60 s).

3.2.2. Simulations with domain decomposition technique

3.2.2.1. Outdoor airflow simulation with a sealed model. As shown in Fig. 1, a simulation analyzing the outdoor domain with a sealed model was required for the DDT simulation to obtain the instantaneous C_p value and instantaneous velocity parallel to the openings. The whole domain model was replaced by a sealed model without openings, and an outdoor simulation was conducted under isothermal conditions. The test model was exposed to a boundary layer flow of 1.0 m/s at a height of 1000 mm from the floor. This velocity was different from the value of 10 m/s used in the wind tunnel experiment. A C_P be noted that 10 m/s in C_P value measurement was used to avoid inaccurate results that could be caused by the unstable operation of the wind tunnel fan and the accuracy of the pressure transducer in the low-pressure range. However, the flow field to be analyzed is under 1.0 m/s. Because issues regarding instability or accuracy range in the experiment were not a problem, 1.0 m/s was adopted in the sealed model simulation in the CFD. Two velocity components parallel to the openings were sampled 7.5 mm away from the center of the assumed opening position of the sealed model wall. Instantaneous static pressure at the center of the assumed opening position. The static pressure at the windward side where the pitot tube was installed in the experiment, was adopted as the reference pressure and monitored during the analysis. The total number of cells was 1,052,170. The same fluctuating turbulent flow used in the whole domain simulation was adopted as the inlet boundary condition. The initial conditions were obtained from the RANS simulation with the same setting as the whole domain simulation. The preconditioning period, which is the transition period from the RANS results to the LES, was set to 20 s. The time for the main calculation period was set to 60 s. The other numerical settings were the same as those of the whole domain simulations. The time step size was set at 0.001 in the pre-conditioning period and the main calculation period.

Table 3
Summary of the whole domain simulation.

CFD Code	Ansys Fluent 2022 R2	
Turblence model	Large Eddy Simulation (Smagorinsky-Lilly Model)	
Algorithm	PISO	
Descretization scheme for advection term	Central differencing	
Time Step	0.001 s (1 kHz)	
Pre-conditioning period	20,000 time steps (20 s)	
Main calculation period	60,000 time steps (60 s)	
Boundary condition (Velocity)	Inlet	Smirnov's method based on experimental value
	Outlet	Gauge pressure: 0 [Pa]
	Walls	Werner and Wengle wall function
Boundary condition (Thermal)	Shown in Table 2 and Fig. 9	
Total number of cells	Whole domain	11,33,140
	Outdoor simulation	10,52,170
	Indoor simulation	1,07,000

3.2.2.2. Indoor airflow simulation using domain decomposition technique. Fig. 9(b) shows the mesh layout of the indoor simulation (i.e., a computational domain of the DDT simulation). The domain measured 300 mm (290 mm + thickness 5 mm × 2 openings) × 290 mm × 295 mm, with the opening surfaces as the inlet and outlet boundaries. The total number of cells was 107,000 cells. In the indoor simulation, the meshing, wall boundary conditions, thermal boundary conditions, and heat flux were the same as those in the whole domain simulation. Fig. 11 (a) and (b) show the instantaneous pressure coefficient and airflow rate (hereinafter referred to as AFR), respectively, as calculated using Eq. (3) in Section 2 and the indoor temperature, which was calculated from the iterative calculation (Fig. 1 Step 2). In the same way as the whole domain simulation, the initial value was calculated by RANS simulation, where the RSM was applied as the turbulence model, and the SIMPLE was applied for pressure–velocity coupling, QUICK was applied for discretization scheme for advection term. Also, the initial indoor temperature was set at 45 °C. The pre-conditioning period, which is the transition period from the RANS simulation results to LES, was set at 20 s. The time for the main calculation period was set to 60 s. The time step size was set at 0.001 s during the simulation. In the pre-conditioning period of DDT, the inflow and outflow wind velocity components calculated from the outdoor simulation were given as the boundary conditions for the pre-conditioning period of DDT. Similarly, the inflow and outflow boundary conditions calculated from the main calculation of the outdoor simulation were given as the boundary conditions for the main simulation period. As mentioned in Section 2, the inflow and outflow boundary wind velocities normal to the opening are calculated by dividing the instantaneous airflow rate by the opening area. These velocities are uniformly distributed over the opening surfaces.

As shown in Fig. 11 (a), the differences in the mean C_p value were 1.06 in Case 1, and 0.96 in Case 2. In Case 2, the instantaneous AFR value was negative at some time steps, which means that the airflow moved from the leeward to the windward direction. This appears to be due to the two opposing driving forces of buoyancy and wind. The variation in the AFR was larger in Case 2 than in Case 1 owing to the instability of the total pressure difference. From these results, it can be concluded that unsteady ventilation occurred in Case 2. Fig. 11(c) shows the three components of the instantaneous velocity obtained from Steps 1(v_{pi1}, v_{pi2}) and 2 (v_{ni}), which are given as the inlet and outlet boundary conditions of these DDT simulations.

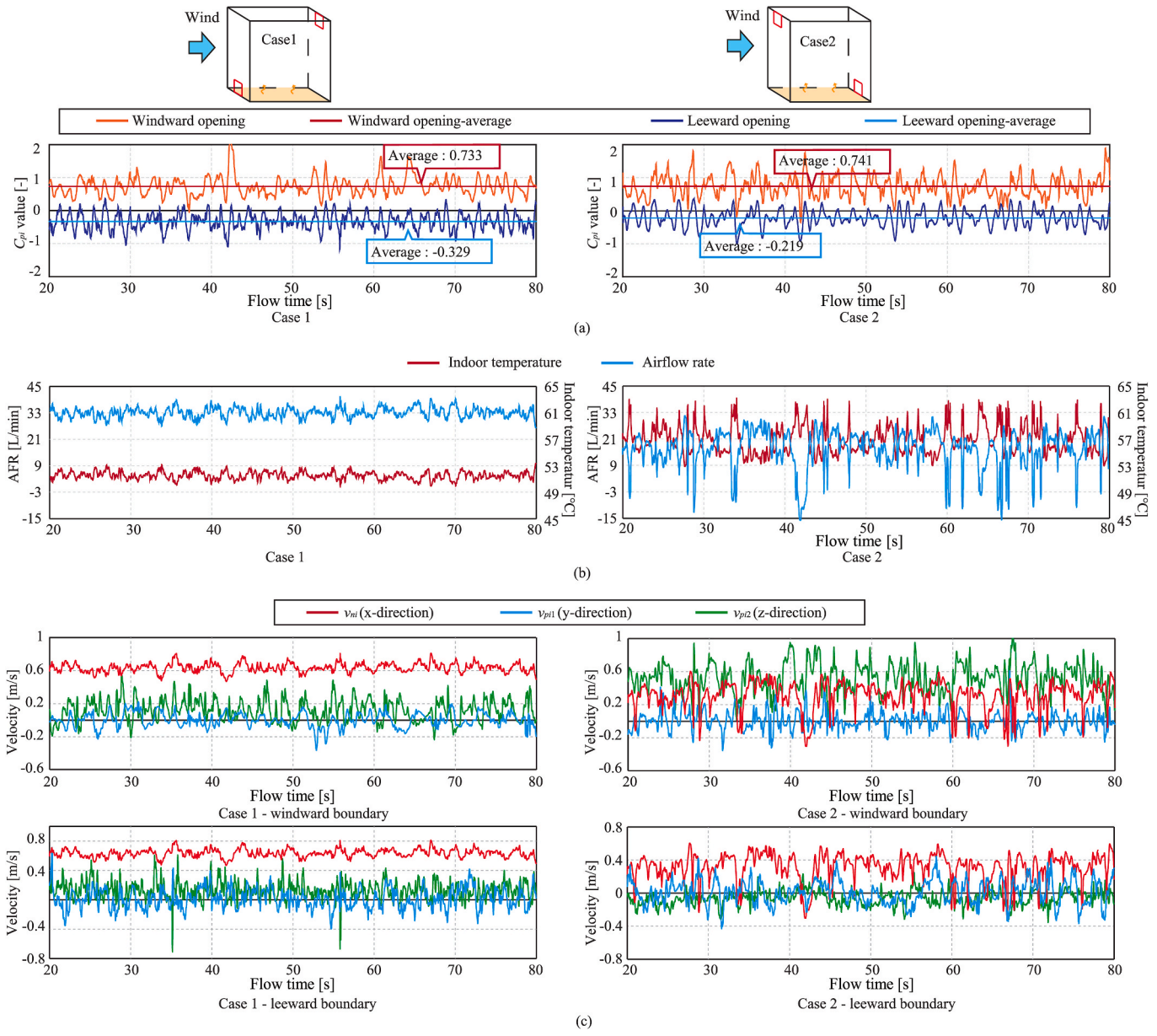

Fig. 11. Results of iterative calculation and boundary condition of indoor simulation: (a) C_{pi} value (used as the ΔC_{pi} in Eq. (4)); (b) instantaneous value of AFR and temperature; (c) instantaneous value of v_{ni}, v_{pi1}, and v_{pi2} (the boundary conditions of the indoor airflow simulation).

4. Results

4.1. CFD validation

To validate the accuracy of the CFD analysis, the results of the wind tunnel experiment were compared with the LES for the whole domain simulation of Case 1 and the outdoor simulation required for the DDT simulation. The outdoor simulation was validated by comparing time-averaged C_p values. For the whole domain simulation, the indoor temperature and indoor velocity distributions obtained by the PIV were compared.

The time-averaged C_p value of the experimental results was compared with those of the outdoor simulation using the sealed model, as shown in Fig. 13(a). In the outdoor simulation, the $\overline{C_{pi}}$ value was calculated using only the time-averaged value of the static pressure during the main simulation period. The root mean square error (hereinafter referred to as RSME) was 0.05. The numerical results for the wind pressure coefficient of the sealed model are in good agreement with the results of the wind tunnel experiment on the windward and leeward walls. Therefore, the LES analysis for the outdoor domain reproduced the experiment.

Fig. 12(b) shows the temperature distribution in the indoor domain. In the experiment, the uniform indoor temperature assumed for similarity calculation shown in Table 1 was 44.6 °C. In the experiment, the temperature at the center of the room was 45.6 °C which is almost the same as the assumed condition. The temperature distribution of CFD in the room generally agrees with the experimental results, however, a difference of approximately 3 °C exists in the leeward part of the room. The RSME was 3 °C.

Fig. 12(c) shows the normalized velocity vectors obtained from the PIV measurement and whole domain calculation (Case 1). The separation flow occurred near the leeward wall in both charts. In the PIV measurement, the inlet airflows along the floor surface, however, in the whole domain simulation, the inlet airflows slightly downward. The flow circulation in the room was counterclockwise in both cases. Near the windward wall, the PIV result was slightly smaller than that of the

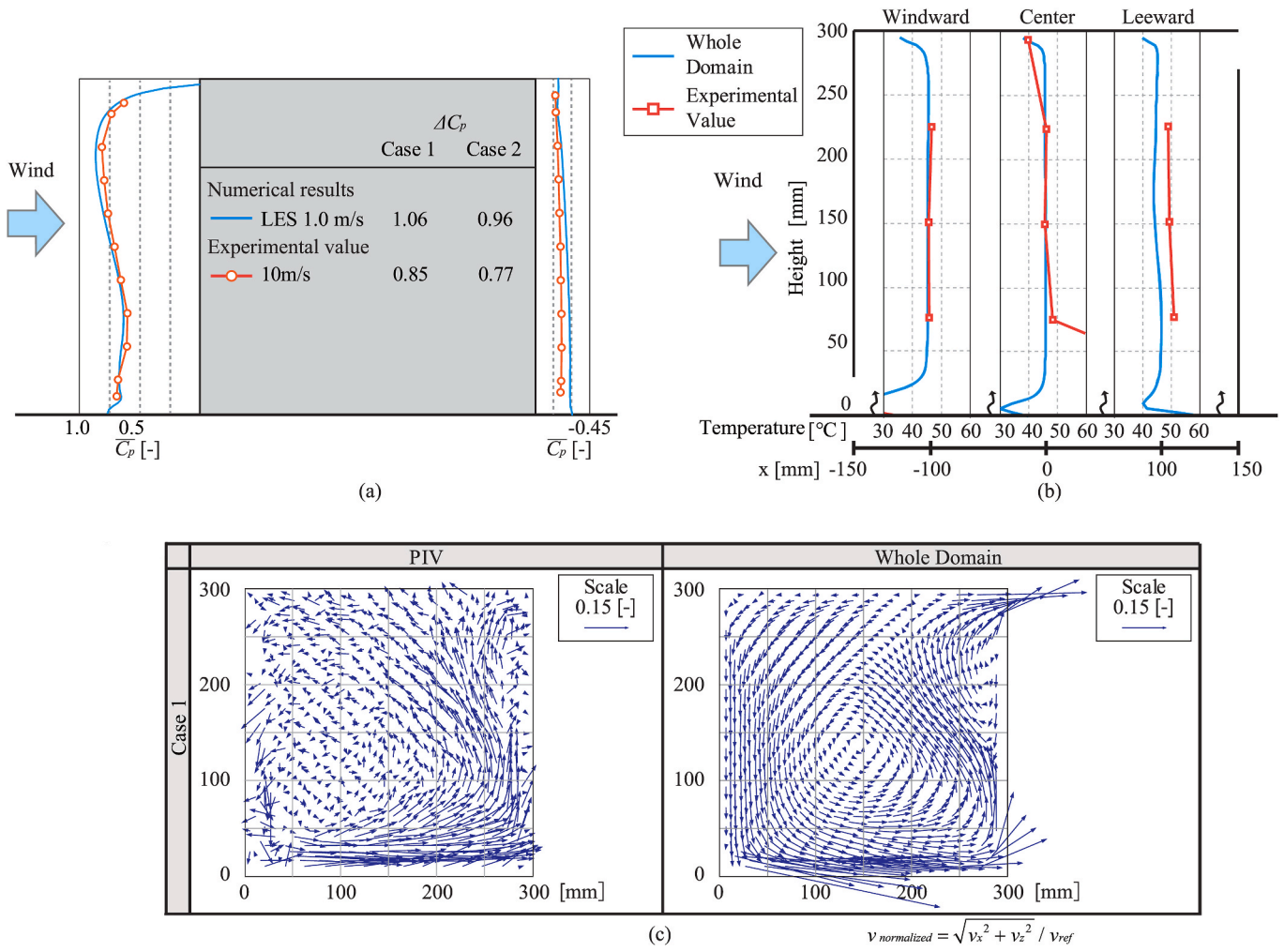

Fig. 12. Validation of whole domain simulation: (a) validation of time-averaged C_p value; (b) validation of vertical temperature distribution; (c) validation of velocity distribution with normalized velocity.

domain simulation. This can be attributed to the reflection effect of the acrylic board during the PIV measurement. Throughout the comparison of the whole domain, both the indoor temperature and indoor flow pattern could be simulated relatively well by the LES.

4.2. Accuracy verification of domain decomposition technique

To investigate the applicability of the DDT and the problems to be solved, the results of the indoor airflow simulation obtained using the DDT were compared with those of the whole domain simulation. The velocity, temperature, AFR, and computational load were compared between the DDT and whole domain simulation. The causes of these differences are discussed.

4.2.1. Velocity distribution

Fig. 13(a) shows a comparison of the time-averaged indoor velocity magnitudes. In Case 1, a separation flow was observed near the leeward wall surface in both the DDT and whole domain simulations. However, the velocity of the separation flow was lower in DDT. The direction of inflow in the whole domain calculation was obliquely downward, whereas it was obliquely upward in the DDT. This may be because the boundary condition for the z-component of the velocity in the DDT was acquired inappropriately. This difference could have been caused by not considering the velocity distribution at the opening. In Case 2, the air velocity distribution at the center of the room was in good agreement. In both cases, the airflow near the windward opening differed from that in the whole domain simulation.

The mean and standard deviations of the velocity magnitude at the monitored points in the room are shown in Fig. 13(b). In the DDT of Case 1, the velocity magnitude was in good agreement, except near the windward opening. The mean wind velocity tends to be evaluated near the opening. In Case 2, there was a slight difference in the wind velocity near the opening on the windward side, but the other parts of the room were in good agreement. In Case 1, dominating flow is generated and the accuracy of the reproduction of the inlet airflow is dominant. On the other hand, Case 2 is an oscillating flow field, with the entire room mixing easily, and the flow in the entire room matches well even when the inlet airflow characteristics are not reproduced precisely. In all cases, the standard deviation was larger near the opening and smaller at the center of the room. In summary, the inflow direction in Case 1 is not well reproduced by DDT, and a more detailed discussion is to be shown in Section 5.

4.2.2. Temperature distribution

The time-averaged temperature distribution in the room in the central cross-section is shown in Fig. 14(a). In the DDT of Case 1, the temperature was lower at the bottom of the room because of the detachment of the inflow air near the floor surface. In both cases, the temperature distributions at the center of the room were almost the same. However, in Case 1, the temperature in the DDT near the inflow opening differed. This is considered to be due to the different inflow wind directions, as well as the wind velocity distribution described

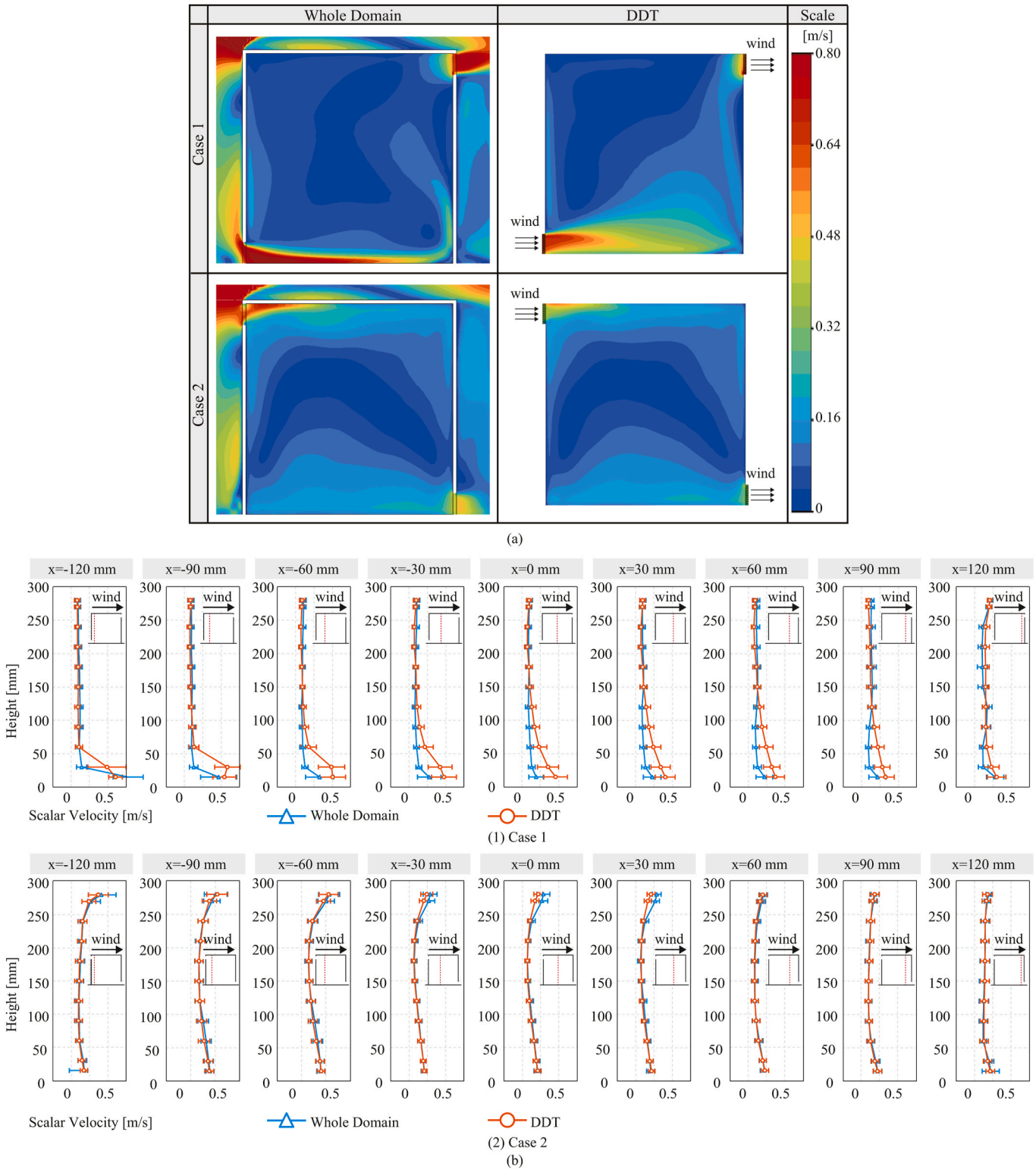

Fig. 13. Validation of velocity: (a) time-averaged velocity distribution contour; (b) validation of scalar velocity and standard deviation.

above. Fig. 14(b) shows the vertical temperature distribution in the room and horizontal surface-averaged values. The indoor temperature was 40–50 °C in most locations in both cases. The vertical temperature distribution in Case 1 is in good agreement with that in the upper part of the room. In Case 2, the temperatures generally agreed at all the points. The horizontal surface-averaged temperatures exhibited good agreement in both cases.

4.2.3. *Airflow rate (AFR)*

The AFR results are presented in Fig. 15. The AFR of the DDT was calculated in Step 2, as shown in Fig. 1, and used as the boundary condition of the simulation. However, in the whole domain simulation, the instantaneous inflow and outflow were calculated at all time steps from the instantaneous velocities normal to the opening obtained at 25 points on each opening surface. The airflow rates were distinguished

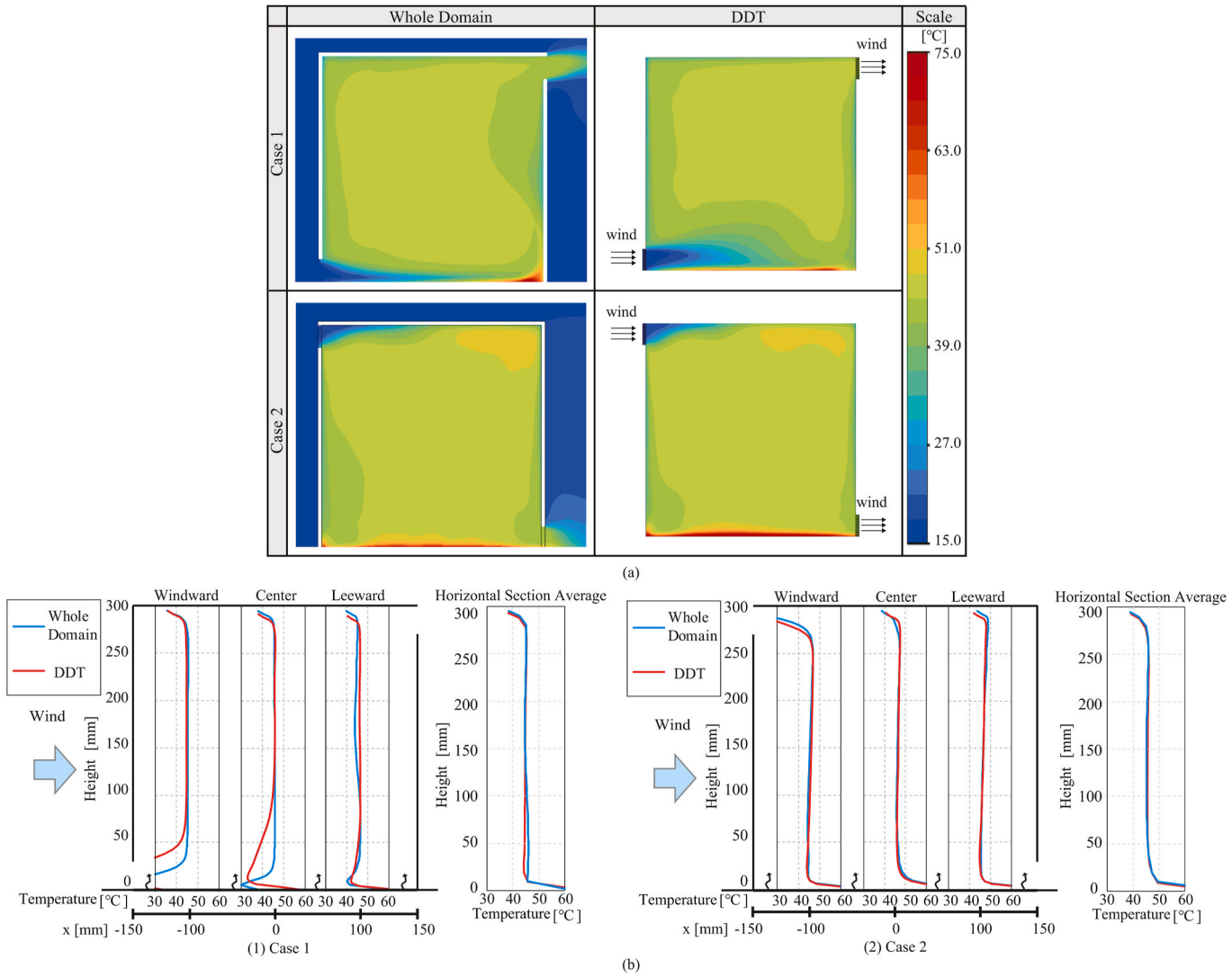

Fig. 14. Validation of temperature: (a) time-averaged temperature distribution contour; (b) vertical temperature distribution.

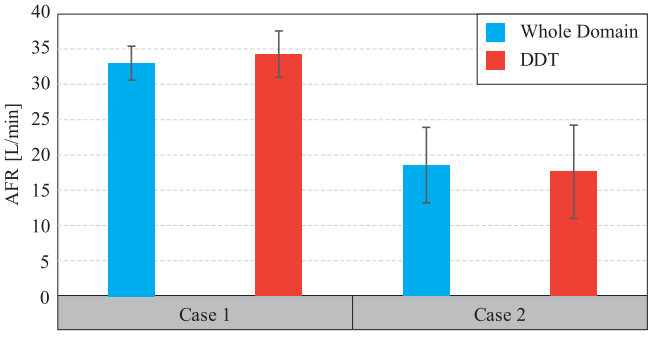

Fig. 15. Validation of AFR

between the inflow and outflow, and the average absolute values were used in Eq. (12) [55].

$$\mathrm{AFR} = \frac{\overline{(|Q_{in\text{-}out}| + |Q_{out\text{-}in}|)}}{2} \tag{12}$$

where AFR is the airflow rate [m^3/s], $Q_{in\text{-}out}$ is the airflow rate from indoor to outdoor [m^3/s], and $Q_{out\text{-}in}$ is the airflow rate from outdoor to indoor. In Case 1 whole domain simulation results in 33.0 ± 2.3 L/min, and the DDT results in 34.3 ± 3.2 L/min. In Case 2 whole domain simulation results in 18.6 ± 5.4 L/min, and the DDT results in 17.6 ± 6.6 L/min. The mean values of the AFR generally matched between the DDT and the whole domain simulations. The standard deviations tended to be slightly larger for the DDT.

4.2.4. *Computational load*

LES simulations were performed on a CPU with Intel Xeon multiple 48-core processors. The calculation times are listed in Table 4. The sealed model simulation (outdoor simulation of DDT) required 130 h to complete. In Case 1, the whole domain simulation required 192 h, whereas the indoor simulation of the DDT required 74 h. In Case 2, the whole domain simulation required 203 h, whereas the indoor simulation of the DDT required 40 h. Consequently, DDT reduced 74 % of the computational load in Case1 and 80 % in Case2. When multiple

Table 4
Computational load.

	Whole domain [h]	DDT [h]	Reduction ratio [%]
Case 1	192	50	74
Case 2	203	40	80
			Outdoor domain
Sealed model			130

simulations are performed during the design phase, the reduction in computational load by DDT becomes even more effective.

5. Discussion

In this study, points 7.5 mm (one-quarter of $A^{0.5}$) from the openings were used as reference points in Step 2 of the DDT calculation procedure [45]. To consider the appropriate reference point of the wind velocity parallel to the openings, other velocity reference points, 15 mm (half of $A^{0.5}$), 22.5 mm (3/4 of $A^{0.5}$), and 30 mm ($A^{0.5}$) from the windows were investigated to determine the appropriate reference point for the wind velocity parallel to the openings. To understand the cause of the error in the DDT, discrete Fourier transformations were conducted using the wind velocities in the z-direction obtained at each point from the outdoor simulation. In the Fourier transformation, a Hanning window is used as the smoothing method. In addition, the turbulent length scales were calculated from the autocorrelation and mean velocity at each point.

Fig. 16 shows a comparison of the power spectrum density and time series fluctuations of the z-direction velocity at the windward opening center and reference points in the outdoor domain in Case 1.

In whole domain simulations, the wind direction was downward, whereas the reference point of 7.5 mm was upward, which was used as the boundary condition. The z-direction wind velocities exhibited a downward wind direction at points other than 7.5 mm in the outdoor simulation. The trends of the power spectrum densities were also similar to the whole domain simulation results except for 7.5 mm. A significant difference was observed in the spectral density at frequencies higher than 10 Hz. This was owing to vortex generation near the bottom of the wall (7.5 mm) caused by the wind falling along the wall and impacting the floor after hitting the wall of the sealed model. The high-frequency spectral density fluctuations also differed because of the impinging flow. Therefore, 22.5 mm and 30 mm exhibited the best agreement with the whole domain result. In the DDT, when an opening exists near the floor, the reference point of the wind velocity components parallel to the window surface should be set back from the wall surface. To investigate the length scale of the vortex at these reference points, the time scales were calculated using auto-correlation coefficients with the composed velocity in the xz-direction at each point. The integral time, turbulent length, and turbulent length scales were calculated using Eqs. (13)–(17). In Eq. (15), integration is interrupted when the autocorrelation coefficient initially falls below zero.

$$\overline{u'(t)u'(\tau)} = \lim_{T\to\infty}\frac{1}{T}\int_0^T u_i'(t)u_i'(t+\tau)dt \tag{13}$$

$$\mathrm{R}(\tau) = \frac{\overline{u'(t)u'(t+\tau)}}{\overline{u'(t)^2}} \tag{14}$$

$$T_I = \int_0^\infty \mathrm{R}(\tau)d\tau \tag{15}$$

$$\Lambda = \overline{u}\cdot T_I \tag{16}$$

$$\lambda = {C_D}^{1/4} \bullet \Lambda \tag{17}$$

where u_i' [m/s] is the instantaneous fluctuating component of velocity, τ [s] is the time lag, R is the autocorrelation coefficient [−], T_I is the integral time scale [s], C_D is the empirical coefficient [−] ($C_D = 0.09$),

Table 5 lists the average velocities, integral time scales, integral turbulent length scales, and turbulent length scales. The integral timescale is 0.26 at all points. The turbulent length scale changed depending on the mean velocity. The smallest turbulence length (26.84 mm at 7.5 mm away from the windward wall was used as the DDT reference point. The turbulence length increased when the distance from the wall until 22.5 mm. In cases where the windward opening was close to the floor, as in this study, there were some influences caused by the small vortex generated by the impinging flow. Therefore, the reference point for velocity parallel to the openings was located away from the wall.

6. Conclusion

The objective of the present study was to explore the applicability of DDT for the indoor airflow simulation of natural ventilation with LES under non-isothermal conditions by comparing it with the whole domain simulation. In this study, a wind tunnel experiment was first conducted to obtain the experimental values of the temperature, airflow characteristics, and wind pressure coefficient for CFD validation. Subsequently, a whole domain simulation was performed to reproduce the experiment. The simulation analyzed both the indoor/outdoor domains simultaneously. To validate the whole domain and outdoor simulations, the wind pressure coefficient, vertical temperature distribution, and indoor airflow pattern were compared with the experimental results. The wind pressure coefficients agreed well at the windward and leeward walls. The temperature from the whole domain simulation was in good agreement with the experimental results. Next, DDT was applied to the LES under two non-isothermal conditions. The velocity distribution, temperature, and AFR of the DDT results are compared with those of the whole domain simulation. There was a difference in wind direction near the windward opening. This may be because the z-direction wind velocity was acquired at an inappropriate point. The vertical temperature distribution matched well except near the opening of the inflow. In both cases, the AFR values and their standard deviations were almost identical to those of the whole domain simulations. Thus, it was shown that the DDT could simulate the airflow distribution, temperature, and AFR with high accuracy. To improve the accuracy of the DDT further, other possible velocity reference points were investigated in the outdoor simulation. The time series of the z component of the velocity and its power spectrum densities at these points were compared with the results of the whole domain simulation. In addition, turbulent length scales were investigated. In this study, DDT reduced more than 70 % of the computational load and simulated non-isothermal cases with high accuracy. However, when using a DDT with an opening near the floor, the reference point for wind velocity parallel to the opening must be away from the wall when using the DDT.

Under the conditions of Case 1, differences were observed in the detailed airflow field near the windward opening, which seems to have been a problem in predicting the inflow airflow direction. If the purpose of the application to practical design is to predict the qualitative indoor airflow and temperature fields or ventilation rate, it could not be a problem, however, further verification under various opening conditions will be necessary. In addition, this study was conducted using an isolated building, and verification should also be conducted under conditions where there are buildings in the surrounding area.

Consequently, the DDT can further reduce the calculation load when opening locations are considered during the natural ventilation design stage. Using DDT with LES, it is possible to apply unsteady analysis to actual buildings with complex geometries during the design phase, thereby enabling a more accurate natural ventilation design.

CRediT authorship contribution statement

Toru Matsubara: Writing – original draft, Validation, Project administration, Methodology, Investigation, Conceptualization. **Tomohiro Kobayashi:** Writing – review & editing, Project administration, Methodology, Funding acquisition, Conceptualization. **Toshio Yamanaka:** Supervision, Methodology, Investigation. **Noriaki Kobayashi:** Methodology. **Narae Choi:** Supervision. **Shohei Miyazawa:** Validation, Project administration, Methodology, Investigation. **Zitao Jiang:** Project administration, Methodology, Investigation. **Chisato Tambara:** Writing – review & editing, Supervision.

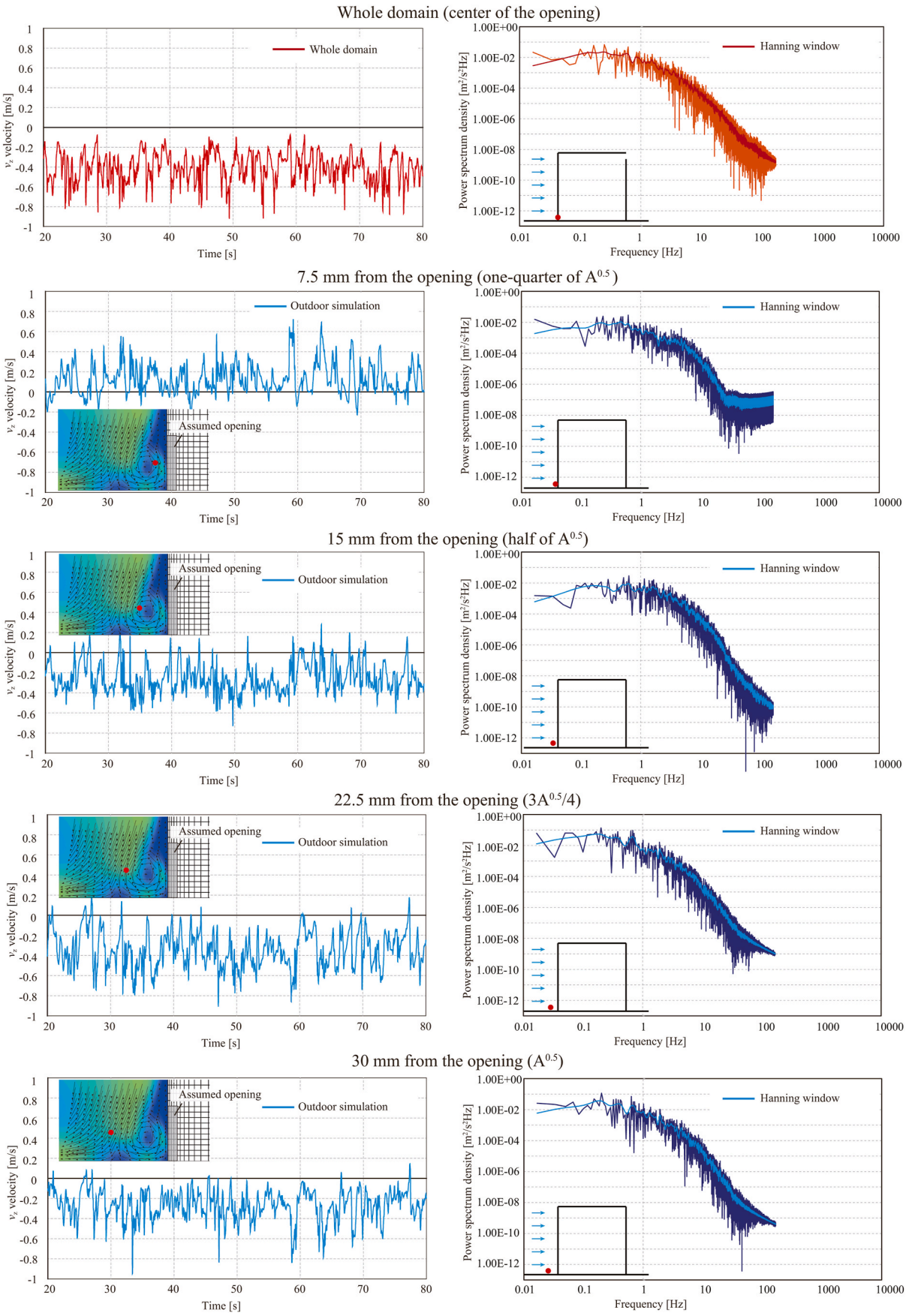

Fig. 16. Time series of z-direction wind velocity and Fourier Power spectrum density for Case 1, windward.

Table 5
Average velocity, time scale, and length scale at the reference point.

Distance from windward wall [mm]	Mean velocity [m/s]	Integral time scale [s]	Integral turbulent length scale [mm]	Turbulent length scale [mm]
7.50	0.19	0.26	49.00	26.84
15.00	0.30		77.10	42.23
22.50	0.38		96.62	52.92
30.00	0.32		83.01	45.47

Declaration of competing interest

This manuscript has not been published or presented elsewhere in part or in entirety and is not under consideration by another journal. We have read and understood your journal's policies, and we believe that neither the manuscript nor the study violates any of these. There are no conflicts of interest to declare.

Data availability

Data will be made available on request.

Acknowledgment

This work was supported by JSPS KAKENHI Grant-in-Aid for Scientific Research in Japan (Grant-in-Aid for Scientific Research(B), Grant Number: 20H02311, Principal Investigator: Tomohiro Kobayashi).

Appendix A. Supplementary data

Supplementary data to this article can be found online at https://doi.org/10.1016/j.buildenv.2024.111763.

References

[1] P.F. Linden, The fluid mechanics of natural ventilation, Annu. Rev. Fluid Mech. 31 (1999) 201–238, https://doi.org/10.1146/annurev.fluid.31.1.201.
[2] P.F. Linden, G.F. Lane-Serff, D.A. Smeed, Emptying filling boxes: the fluid mechanics of natural ventilation, J. Fluid Mech. 212 (1990) 309–335, https://doi.org/10.1017/S0022112090001987.
[3] J. Lim, Y. Akashi, R. Ooka, H. Kikumoto, Y. Choi, A probabilistic approach to the energy-saving potential of natural ventilation: effect of approximation method for approaching wind velocity, Build. Environ. 122 (2017) 94–104, https://doi.org/10.1016/j.buildenv.2017.06.008.
[4] J. Pu, Y. Yuan, F. Jiang, K. Zheng, K. Zhao, Buoyancy-driven natural ventilation characteristics of thermal corridors in industrial buildings, J. Build. Eng. 50 (2022) 104107, https://doi.org/10.1016/j.jobe.2022.104107.
[5] H.L. Gough, Z. Luo, C.H. Halios, M.-F. King, C.J. Noakes, C.S.B. Grimmond, J. F. Barlow, R. Hoxey, A.D. Quinn, Field measurement of natural ventilation rate in an idealised full-scale building located in a staggered urban array: comparison between tracer gas and pressure-based methods, Build. Environ. 137 (2018) 246–256, https://doi.org/10.1016/j.buildenv.2018.03.055.
[6] L.J. Lo, A. Novoselac, Cross ventilation with small openings: measurements in a multi-zone test building, Build. Environ. 57 (2012) 377–386, https://doi.org/10.1016/j.buildenv.2012.06.009.
[7] A. Mochida, H. Yoshino, T. Takeda, T. Kakegawa, S. Miyauchi, Methods for controlling airflow in and around a building under cross-ventilation to improve indoor thermal comfort, J. Wind Eng. Ind. Aerod. 93 (2005) 437–449, https://doi.org/10.1016/j.jweia.2005.02.003.
[8] H. Pabiou, J. Salort, C. Ménézo, F. Chillà, Natural cross-ventilation of buildings, an experimental study, Energy Proc. 78 (2015) 2911–2916, https://doi.org/10.1016/j.egypro.2015.11.666.
[9] A. Tablada, F. De Troyer, B. Blocken, J. Carmeliet, H. Verschure, On natural ventilation and thermal comfort in compact urban environments – the Old Havana case, Build. Environ. 44 (2009) 1943–1958, https://doi.org/10.1016/j.buildenv.2009.01.008.
[10] C.R. Chu, Y.-H. Chiu, Y.-J. Chen, Y.-W. Wang, C.-P. Chou, Turbulence effects on the discharge coefficient and mean flow rate of wind-driven cross-ventilation, Build. Environ. 44 (2009) 2064–2072, https://doi.org/10.1016/j.buildenv.2009.02.012.
[11] P. Heiselberg, M. Sandberg, Evaluation of discharge coefficients for window openings in wind driven natural ventilation, Int. J. Vent. 5 (2006) 43–52, https://doi.org/10.1080/14733315.2006.11683723.
[12] P. Karava, T. Stathopoulos, A.K. Athienitis, Airflow assessment in cross-ventilated buildings with operable façade elements, Build. Environ. 46 (2011) 266–279, https://doi.org/10.1016/j.buildenv.2010.07.022.
[13] N. Ikegaya, S. Hasegawa, A. Hagishima, Time-resolved particle image velocimetry for cross-ventilation flow of generic block sheltered by urban-like block arrays, Build. Environ. 147 (2019) 132–145, https://doi.org/10.1016/j.buildenv.2018.10.015.
[14] M. Shirzadi, Y. Tominaga, P.A. Mirzaei, Wind tunnel experiments on cross-ventilation flow of a generic sheltered building in urban areas, Build. Environ. 158 (2019) 60–72, https://doi.org/10.1016/j.buildenv.2019.04.057.
[15] S. Kato, S. Murakami, A. Mochida, S. Akabayashi, Y. Tominaga, Velocity-pressure field of cross ventilation with open windows analyzed by wind tunnel and numerical simulation, J. Wind Eng. Ind. Aerod. 44 (1992) 2575–2586, https://doi.org/10.1016/0167-6105(92)90049-G.
[16] T. van Hooff, B. Blocken, L. Aanen, B. Bronsema, A venturi-shaped roof for wind-induced natural ventilation of buildings: wind tunnel and CFD evaluation of different design configurations, Build. Environ. 46 (2011) 1797–1807, https://doi.org/10.1016/j.buildenv.2011.02.009.
[17] A. Sugahara, H. Kotani, Y. Momoi, T. Yamanaka, K. Sagara, R. Fujiwara, PIV measurement and CFD analysis of airflow around building roof with various building installations, Int. J. Vent. 16 (2017) 163–173, https://doi.org/10.1080/14733315.2017.1299513.
[18] L.A.A. Stamatios Katotakis, Numerical Solution of the Laminar Boundary Layer Equations, 1969, p. 142.
[19] B. van Leer, Towards the ultimate conservative difference scheme. V. A second-order sequel to Godunov's method, J. Comput. Phys. 32 (1979) 101–136, https://doi.org/10.1016/0021-9991(79)90145-1.
[20] P. Woodward, P. Colella, The numerical simulation of two-dimensional fluid flow with strong shocks, J. Comput. Phys. 54 (1984) 115–173, https://doi.org/10.1016/0021-9991(84)90142-6.
[21] M.F. Doherty, J.D. Perkins, On the dynamics of distillation processes—IV Uniqueness and stability of the steady state in homogeneous continuous distillations, Chem. Eng. Sci. 37 (1982) 381–392, https://doi.org/10.1016/0009-2509(82)80090-0.
[22] A. Jameson, Analysis and design of numerical schemes for gas dynamics 1, artificial diffusion, upwind biasing, limiters and their effect on multigrid convergence. RIACS Technical Report No. 94.15, Int. J. Comput. Fluid Dynam. 4 (1995) 171–218, https://doi.org/10.1080/10618569508904524.
[23] B.E. Launder, D.B. Spalding, The numerical computation of turbulent flows, Comput. Methods Appl. Mech. Eng. 3 (1974) 269–289, https://doi.org/10.1016/0045-7825(74)90029-2.
[24] B. Blocken, LES over RANS in building simulation for outdoor and indoor applications: a foregone conclusion? Build. Simul. 11 (2018) 821–870, https://doi.org/10.1007/s12273-018-0459-3.
[25] J. Smagorinsky, General circulation experiments with the primitive equations: I. The basic experiment, Mon. Weather Rev. 91 (1963) 99–164, https://doi.org/10.1175/1520-0493(1963)091<0099:GCEWTP>2.3.CO;2.
[26] U. Piomelli, Large eddy simulations in 2030 and beyond, Phil. Trans. Math. Phys. Eng. Sci. 372 (2014) 20130320, https://doi.org/10.1098/rsta.2013.0320.
[27] Y. Zhiyin, Large-eddy simulation: past, present and the future, Chin. J. Aeronaut. 28 (2015) 11–24, https://doi.org/10.1016/j.cja.2014.12.007.
[28] T. Okaze, H. Kikumoto, H. Ono, M. Imano, N. Ikegaya, T. Hasama, K. Nakao, T. Kishida, Y. Tabata, K. Nakajima, R. Yoshie, Y. Tominaga, Large-eddy simulation of flow around an isolated building: a step-by-step analysis of influencing factors on turbulent statistics, Build. Environ. 202 (2021) 108021, https://doi.org/10.1016/j.buildenv.2021.108021.
[29] H.C. Lim, T.G. Thomas, I.P. Castro, Flow around a cube in a turbulent boundary layer: LES and experiment, J. Wind Eng. Ind. Aerod. 97 (2009) 96–109, https://doi.org/10.1016/j.jweia.2009.01.001.
[30] P. Gousseau, B. Blocken, G.J.F. van Heijst, Quality assessment of Large-Eddy Simulation of wind flow around a high-rise building: validation and solution verification, Computers & Fluids 79 (2013) 120–133, https://doi.org/10.1016/j.compfluid.2013.03.006.
[31] D.A. Köse, E. Dick, Prediction of the pressure distribution on a cubical building with implicit LES, J. Wind Eng. Ind. Aerod. 98 (2010) 628–649, https://doi.org/10.1016/j.jweia.2010.06.004.
[32] G. Jiang, R. Yoshie, T. Shirasawa, X. Jin, Inflow turbulence generation for large eddy simulation in non-isothermal boundary layers, J. Wind Eng. Ind. Aerod. (2012) 369–378, https://doi.org/10.1016/j.jweia.2012.02.030, 104–106.
[33] H. Cheng-Hu, T. Kurabuchi, M. Ohbal, Numerical study of cross-ventilation using two-equation RANS, Int. J. Vent. 4 (2005) 123–131, https://doi.org/10.1080/14733315.2005.11683704.
[34] Y. Cheng, F.S. Lien, E. Yee, R. Sinclair, A comparison of large Eddy simulations with a standard k–ε Reynolds-averaged Navier–Stokes model for the prediction of a fully developed turbulent flow over a matrix of cubes, J. Wind Eng. Ind. Aerod. 91 (2003) 1301–1328, https://doi.org/10.1016/j.jweia.2003.08.001.
[35] E.R. Meinders, K. Hanjalić, Vortex structure and heat transfer in turbulent flow over a wall-mounted matrix of cubes, Int. J. Heat Fluid Flow 20 (1999) 255–267, https://doi.org/10.1016/S0142-727X(99)00016-8.
[36] Z. Xie, I.P. Castro, LES and RANS for turbulent flow over arrays of wall-mounted obstacles, Flow Turbulence Combust 76 (2006) 291–312, https://doi.org/10.1007/s10494-006-9018-6.
[37] I.P. Castro, H. Cheng, R. Reynolds, Turbulence over urban-type roughness: deductions from wind-tunnel measurements, Boundary-Layer Meteorol. 118 (2006) 109–131, https://doi.org/10.1007/s10546-005-5747-7.
[38] X. Zheng, H. Montazeri, B. Blocken, CFD simulations of wind flow and mean surface pressure for buildings with balconies: comparison of RANS and LES, Build. Environ. 173 (2020) 106747, https://doi.org/10.1016/j.buildenv.2020.106747.

[39] Y. Tominaga, T. Stathopoulos, Numerical simulation of dispersion around an isolated cubic building: model evaluation of RANS and LES, Build. Environ. 45 (2010) 2231–2239, https://doi.org/10.1016/j.buildenv.2010.04.004.
[40] W.-W. Li, R.N. Meroney, Gas dispersion near a cubical model building. Part I. Mean concentration measurements, J. Wind Eng. Ind. Aerod. 12 (1983) 15–33, https://doi.org/10.1016/0167-6105(83)90078-8.
[41] Y. Adachi, N. Ikegaya, H. Satonaka, A. Hagishima, Numerical simulation for cross-ventilation flow of generic block sheltered by urban-like block array, Build. Environ. 185 (2020) 107174, https://doi.org/10.1016/j.buildenv.2020.107174.
[42] S.B. Pope, Turbulent Flows, Higher Education from, Cambridge University Press, 2000, https://doi.org/10.1017/CBO9780511840531.
[43] S. Rezaeiravesh, T. Mukha, M. Liefvendahl, Systematic study of accuracy of wall-modeled large eddy simulation using uncertainty quantification techniques, Computers & Fluids 185 (2019) 34–58, https://doi.org/10.1016/j.compfluid.2019.03.025.
[44] T. Endo, T. Kurabuchi, T. Nonaka, M. Ishii, M. Ohba, T. Goto, Y. Akamine, Development of a simulator for indoor airflow distribution in a cross-ventilated building using the local dynamic similarity model, Int. J. Vent. 5 (2006) 31–42, https://doi.org/10.1080/14733315.2006.11683722.
[45] T. Kurabuchi, M. Ohba, T. Nonaka, Domain decomposition technique applied to the evaluation of cross-ventilation performance of opening positions of a building, Int. J. Vent. 8 (2009) 207–217, https://doi.org/10.1080/14733315.2009.11683846.
[46] T. Kurabuchi, M. Ohba, T. Endo, Y. Akamine, F. Nakayama, Local dynamic similarity model of cross-ventilation Part 1 - theoretical framework, Int. J. Vent. 2 (2004) 371–382, https://doi.org/10.1080/14733315.2004.11683679.
[47] M. Ohba, T. Kurabuchi, T. Endo, Y. Akamine, M. Kamata, A. Kurahashi, Local dynamic similarity model of cross-ventilation Part 2 - application of local dynamic similarity model, Int. J. Vent. (2004), https://doi.org/10.1080/14733315.2004.11683680.
[48] D.W. Etheridge, M. Sandberg, A simple parametric study of ventilation, Build. Environ. 19 (1984) 163–173, https://doi.org/10.1016/0360-1323(84)90023-4.
[49] Y. Li, A. Delsante, Natural ventilation induced by combined wind and thermal forces, Build. Environ. 36 (2001) 59–71, https://doi.org/10.1016/S0360-1323(99)00070-0.
[50] M. Li, Z. Gao, J. Ji, H. Wan, External wind effect on flame behavior inside and outside a compartment with opposing openings, Fire Technol. 57 (2021) 1987–2006, https://doi.org/10.1007/s10694-021-01104-2.
[51] M.S. Davies Wykes, E. Chahour, P.F. Linden, The effect of an indoor-outdoor temperature difference on transient cross-ventilation, Build. Environ. 168 (2020) 106447, https://doi.org/10.1016/j.buildenv.2019.106447.
[52] J. Yuan, L.R. Glicksman, Transitions between the multiple steady states in a natural ventilation system with combined buoyancy and wind driven flows, Build. Environ. 42 (2007) 3500–3516, https://doi.org/10.1016/j.buildenv.2006.10.045.
[53] R.H. Kraichnan, Diffusion by a random velocity field, Phys. Fluid. 13 (1970) 22–31, https://doi.org/10.1063/1.1692799.
[54] S. Shi Smirnov, I. Celik, Random flow generation technique for large eddy simulations and particle-dynamics modeling, J. Fluid Eng. 123 (2001) 359, https://doi.org/10.1115/1.1369598.
[55] T. Kobayashi, M. Sandberg, T. Fujita, E. Lim, N. Umemiya, Numerical analysis of wind-induced natural ventilation for an isolated cubic room with two openings under small mean wind pressure difference, Build. Environ. 226 (2022) 109694, https://doi.org/10.1016/j.buildenv.2022.109694.